

3D Band Diagram and Photoexcitation of 2D–3D Semiconductor Heterojunctions

Bo Li,[†] Gang Shi,[†] Sidong Lei,[†] Yongmin He,^{†,‡} Weilu Gao,^{§,||} Yongji Gong,[⊥] Gonglan Ye,[†] Wu Zhou,[#] Kuntal Keyshar,[†] Ji Hao,[∇] Pei Dong,[†] Liehui Ge,[†] Jun Lou,[†] Junichiro Kono,^{*,†,§,||} Robert Vajtai,^{*,†} and Pulickel M. Ajayan^{*,†}

[†]Department of Materials Science and NanoEngineering, [§]Department of Electrical and Computer Engineering, ^{||}Department of Physics and Astronomy, and [⊥]Department of Chemistry, Rice University, Houston, Texas 77005, United States

[‡]School of Physical Science and Technology, Lanzhou University, Lanzhou, Gansu 730000, P. R. China

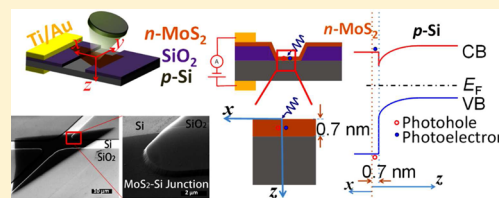
[#]Materials Science and Technology Division, Oak Ridge National Laboratory, Oak Ridge, Tennessee 37831, United States

[∇]Department of Mechanical and Industrial Engineering, Northeastern University, Boston, Massachusetts 02115, United States

Supporting Information

ABSTRACT: The emergence of a rich variety of two-dimensional (2D) layered semiconductor materials has enabled the creation of atomically thin heterojunction devices. Junctions between atomically thin 2D layers and 3D bulk semiconductors can lead to junctions that are fundamentally electronically different from the covalently bonded conventional semiconductor junctions. Here we propose a new 3D band diagram for the heterojunction formed between n-type monolayer MoS₂ and p-type Si, in which the conduction and valence band-edges of the MoS₂ monolayer are drawn for both stacked and in-plane directions. This new band diagram helps visualize the flow of charge carriers inside the device in a 3D manner. Our detailed wavelength-dependent photocurrent measurements fully support the diagrams and unambiguously show that the band alignment is type I for this 2D–3D heterojunction. Photogenerated electron–hole pairs in the atomically thin monolayer are separated and driven by an external bias and control the “on/off” states of the junction photodetector device. Two photoresponse regimes with fast and slow relaxation are also revealed in time-resolved photocurrent measurements, suggesting the important role played by charge trap states.

KEYWORDS: MoS₂–Si heterojunction, band diagram, exciton relaxation, charge generation



The rise of two-dimensional (2D) layered semiconductors has brought about new opportunities of fundamental research in physics, chemistry, and materials science as well as potential applications in optoelectronics and electronics.^{1–22} A 2D atomic layer can be easily deposited on a three-dimensional (3D) crystal, forming a van der Waals (vdW) heterojunction.^{23–31} The vdW nature of heterointerfaces allows one to combine lattice-mismatched materials, lifting conventional limitations of epitaxial growth of covalently bonded III–V heterostructures, significantly increasing the variety of materials. At the same time, new questions and challenges arise in describing electronic states, charge generation, transport, and doping in device structures based on vdW heterostructures. For example, to what degree can one apply the usual effective-mass, envelope-function formalism to atomically thin layers? How should one treat charge transfer that would normally lead to band bending and depletion layers in ordinary p–n junctions? Most notably, due to the atomically thin nature of 2D materials, no spatial region exists to accommodate the formation of a depletion layer in the vertical direction of the stacked structure.² Currently, no established procedures exist for drawing band diagrams for vdW heterojunctions in a realistic and quantitative manner. In most previous studies, 2D

monolayers were simply treated as bulk layers (albeit with monolayer band gaps); band offsets were introduced in an ad hoc manner; optical band gaps (which have strong excitonic shifts from the true band gaps) were used; and no distinction was made between different spatial directions in 3D devices containing 2D–3D heterointerfaces.^{25–31} Systematic studies are needed to elucidate these points for better understanding and further development of vdW heterostructure devices.

In this paper, we describe the fabrication and optoelectronic measurements of a photodetector based on a heterojunction between n-type monolayer MoS₂ and p-type bulk Si, a prototypical 2D–3D p–n heterostructure. Spatial mapping of photocurrent confirms that the observed photosignal is due to carrier generation at the MoS₂–Si heterojunction. Furthermore, based on the wavelength dependence and bias dependence of the photosignal, we propose a novel band diagram that depicts band bending and charge flow in a 3D manner. This diagram allows us to visualize detailed charge generation, separation, and flow dynamics in the whole system, taking into account the p–

Received: May 21, 2015

Revised: July 29, 2015

Published: August 17, 2015

n junction device, substrate, contacts, and the entire circuit. Our data fully support the type I band alignment between the two materials; i.e., the bottom (top) of the conduction (valence) band of MoS₂ lies higher (lower) than that of Si. Finally, time-resolved photocurrent measurements reveal two time scales, which we discuss in terms of charge trapping by defects induced by the oxide separating the MoS₂ layer from Si near one of the contacts.

To fabricate the MoS₂-Si photodetector, we first patterned a SiO₂/p-Si substrate to selectively remove the thermal oxide by a buffered oxide etchant (BOE 10:1) to create a trench and expose the fresh surface of the p-type Si wafer (sheet resistance $2.2 \pm 0.2 \Omega/\square$ and resistivity $0.16 \Omega\text{-cm}$), as shown in Figure 1a, panel i. We then transferred a chemical vapor deposition

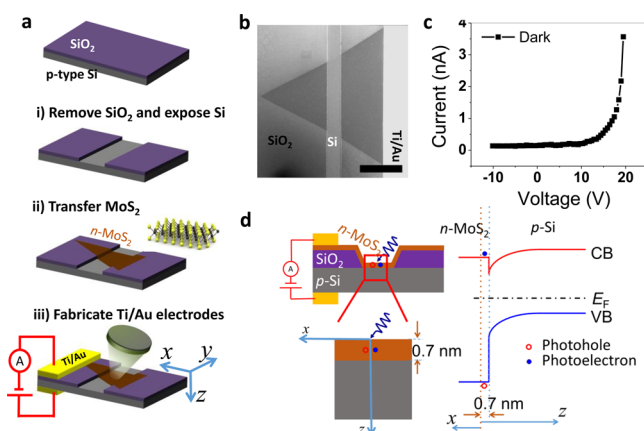


Figure 1. MoS₂-Si heterojunction and band diagram. (a) Schematics showing the fabrication process of the MoS₂-Si heterojunction. The coordinates are defined such that the *z* axis is in the stacking (vertical) direction of the heterojunction, the *x* axis is perpendicular to the exposed Si trench, and the *y* axis is along the Si trench. (b) SEM image of the MoS₂-Si junction device with a Ti/Au contact pad. The exposed Si surface in the trench shows brighter contrast. (c) A representative *I*-*V* characteristic of the device without illumination. (d) A cross-sectional schematic (*x*-*z* plane) of the heterojunction (left), together with a band diagram of the 2D-3D heterojunction along the *x*- and *z*-axes at zero bias under laser excitation. CB: conduction band, and VB: valence band. As shown in the enlarged cross-sectional view, the *z* axis starts from the top of the MoS₂ monolayer (the origin), pointing from MoS₂ to Si. In the band diagram, we draw the bands of MoS₂ in both the vertical direction (*z* direction) and in-plane direction (*x* direction).

(CVD) grown, single-crystal flake of monolayer MoS₂ onto the trench; see Figure 1a, panel ii. One contact pad (Ti/Au) was attached to one side of the MoS₂ flake located on SiO₂, and the other contact was attached to the Si substrate; see Figure 1a, panel iii, and Figure S1. Figure 1b shows a scanning electron microscopy (SEM) image of the device. A representative diode-like *I*-*V* curve with no light illumination is shown in Figure 1c.

To properly model the photoresponse of this heterostructure device in a 3D manner, we introduce a coordinate system, shown in Figure 1a and d. Here the *z*-axis is along the stacking (vertical) direction of the heterojunction, and the *x*- and *y*-axes are defined in the 2D plane of MoS₂. Figure 1d shows a cross-sectional schematic of the device (in the *x*-*z* plane), where the origin of the coordinate system, (*x*, *z*) = (0,0), is located at the top surface of the MoS₂ layer in the middle of the trench. Note that the thickness of the MoS₂ monolayer (only 0.7 nm in reality) is exaggerated. Photogenerated carriers (electrons and

holes) can move both along the vertical (*z*) direction (e.g., flowing from bulk Si into the MoS₂ monolayer) and in the lateral (*x*-*y*) direction (e.g., driven by an in-plane electrical field). A band diagram is shown in Figure 1d, right panel, for the (n)MoS₂-(p)Si heterojunction device in equilibrium under zero bias. Here the conduction band (CB) edge and the valence band (VB) edge are drawn along the *x*-axis and *z*-axis. We are using the quasi-particle band gap (as opposed to the optical band gap, which is reduced by the excitonic shift) for the band gap of MoS₂ (2.27 eV³²). From calculated electron affinities of MoS₂³³ and Si (4.05 eV),³⁴ it is expected that there is a large band offset in the VB. On the other hand, the sign and value of the CB offset have not been determined, and as a result, both type I^{28,29} and type II^{25,27} diagrams have been used in previous studies. Here we are assuming that the band alignment is type I, which is confirmed by the wavelength-dependent photocurrent measurements discussed later.

By controlling and optimizing CVD growth parameters, we were able to synthesize both triangular-shaped monolayer MoS₂ single crystals (Figure 2a) and large-scale monolayer MoS₂ thin film (Figure 2b). The atomic force microscopy (AFM) image shown in Figure 2c, along with the inserted height profile captured from the edge of the film (thickness = 0.66 nm), confirms single-layered uniformity across the entire film. The high-resolution scanning transmission electron microscopy (STEM) image in Figure 2d further proves the monolayer nature of MoS₂; the hexagonal lattice structure with alternating atomic arrangements of Mo and S testifies the high-quality of the MoS₂ layer. Furthermore, it is important to note that these MoS₂ monolayers are highly flexible. Figure 2e and f shows SEM images of a MoS₂ monolayer on a SiO₂/Si substrate with a cross-shaped trench pattern. The magnified image of the SiO₂ step (height = 285 nm) in Figure 2f clearly demonstrates a conformal contact between the MoS₂ monolayer and the three-dimensionally patterned SiO₂/Si substrate. A photoluminescence (PL) map and representative PL spectra of the films are shown in Figure 2g and h, respectively. The PL map in Figure 2g illustrates a significant reduction of PL intensity in the MoS₂-Si junction area, whereas the PL spectra (Figure 2h) of MoS₂ on both SiO₂ and Si show almost the same peak locations and the full width at half-maximum (fwhm), comparable to results reported for MoS₂ obtained by mechanical exfoliation methods.²⁵ The PL intensity reduction of ~87% in the heterojunction area occurs without peak shifting, indicating that p-Si quenches the PL without changing the band gap of MoS₂. Similar phenomena have been observed in other vdW heterostructure p-n junctions such as (n)MoS₂-(p)WSe₂,^{2,35} and (n)MoS₂-(p⁺)Si heterostructures²⁵ and in Raman mapping of the same sample (Supporting Information, Figure S2).

We observed photosignal in the fabricated device only when light illuminated the MoS₂-Si heterojunction area. We performed photocurrent mapping within a $20 \times 20 \mu\text{m}^2$ square area (Figure 3a) under reversed bias (-0.5 V) and forward bias (0.5 V), as shown in Figure 3b and c, respectively. The device was excited by a continuous-wave (CW) 514 nm laser beam focused to a spot of 2 μm in diameter, and the induced photocurrent was collected. Photoresponse can be only seen at the MoS₂-Si heterojunction, under both reverse and forward bias, and a perfect match exists between the photoresponsive region in the photomap and the trench region in the corresponding optical image. Importantly, there is no photosignal observed when the laser beam hits MoS₂ on SiO₂. These

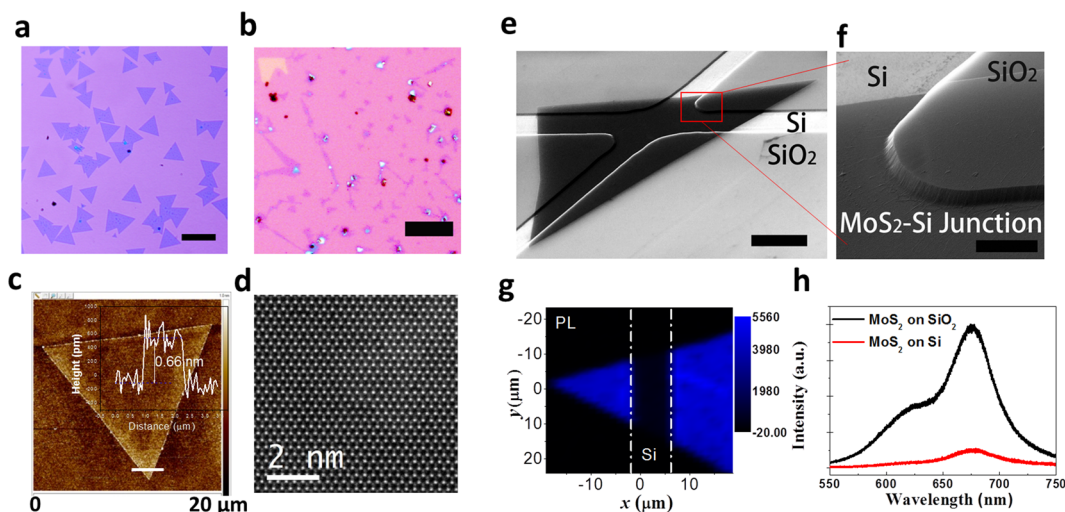


Figure 2. Characterizations of as-grown MoS₂ monolayer and MoS₂-Si heterojunction. Optical images of as-grown (a) MoS₂ monolayer flakes and (b) continuous film on SiO₂/Si substrate. (c) Atomic force microscopy image of triangular shaped monolayer MoS₂. (d) High-resolution TEM image of the MoS₂ lattice. (e) Tilted-angle SEM image of a MoS₂ flake transferred onto a cross-shaped Si pattern, showing continuous MoS₂ at the edge of the SiO₂ steps (285 nm in thickness). (f) Enlarged SEM image of MoS₂ on the edge of a SiO₂ step. (g) Photoluminescence intensity map of the MoS₂-Si junction and (h) representative photoluminescence spectra of MoS₂ on Si and on SiO₂. Scale bars: 100 μm for (a) and (b), 2 nm for (d), 10 μm for (e), and 2 μm for (f).

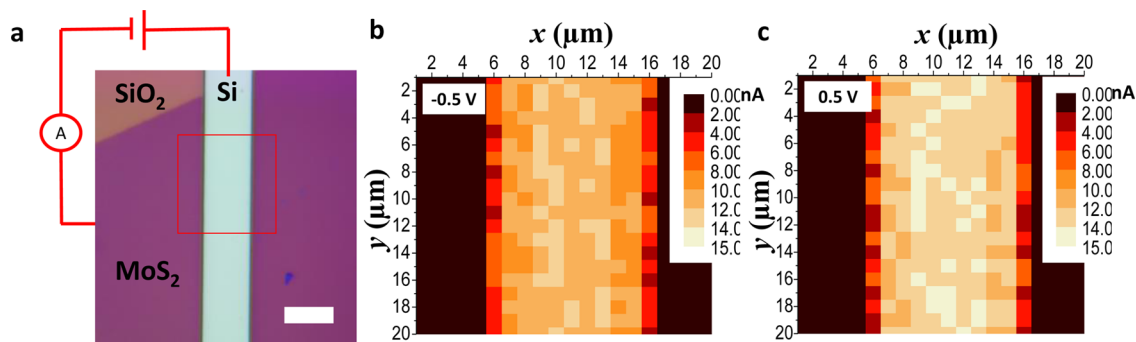


Figure 3. Photocurrent mapping of the MoS₂-Si heterojunction using a CW laser (514 nm). (a) An optical image of the device; scale bar = 10 μm . Photocurrent mapping was performed in (b) a 20 μm \times 20 μm area (corresponding to the red square in a) with a reverse bias (-0.5 V) and (c) a forward bias (+0.5 V).

observations suggest that the photodetection mechanism is related to photogeneration of charge carriers at the MoS₂-Si p-n junction and subsequent electron-hole separation.

To provide more insight into the photodetection mechanism in this heterojunction-based photodetector, we performed wavelength-dependent photocurrent measurements using three CW lasers having different wavelengths: 514, 633, and 785 nm. The powers of the lasers were fixed at ~ 10 nW. We focused the laser beam onto the middle of the trench where the MoS₂-Si heterojunction exists. The I - V characteristics of the device under illumination by different-wavelength laser beams are shown in Figure 4b. Current is observed when the device is illuminated with 514 nm (or 2.41 eV; dark line) and 633 nm (or 1.96 eV; red line) light; no detectable current was present when the device was excited by a 785 nm laser, as shown as the green line, which overlaps the dark current (blue dashed line). The photon energy of 785 nm light, 1.58 eV, is lower than the optical gap of MoS₂ at room temperature (~ 1.9 eV), although it is larger than the room-temperature band gap of Si (~ 1.1 eV). Figure 4c shows more detailed wavelength dependence of the photocurrent at a bias of -1 V from 1000 nm (1.24 eV) to 400 nm (3.1 eV). This photocurrent spectrum unambiguously

shows that direct photocarrier generation in the MoS₂ layer is crucial for the existence of a photocurrent; i.e., photocurrent is finite only when the photon energy is higher than the room-temperature optical gap of MoS₂. Once the photon energy of the incident light is above the optical gap of MoS₂, the device is turned "on", and the photocurrent increases with increasing bias in both directions. Both the wavelength dependence and bias dependence can be successfully explained using our proposed band diagrams, as discussed below.

We developed comprehensive band diagrams for understanding charge generation, separation, and transport processes in this device in a 3D manner, as shown in Figure 4e-p. Figures 4e, f, and g depict the CB (red) and VB (blue) edges of MoS₂ as a function of x and y , while Figure 4h-p show them as a function of x and z . The x -dependence of the MoS₂ bands (at $y = z = 0$) contains singularities due to the sudden substrate change (from Si to SiO₂) as well as the metallic contact at the end; they influence the transport of charge carriers in the plane of the MoS₂ monolayer. Vertical (z) transport, on the other hand, is determined by the MoS₂-Si junction, which is depicted in Figure 4h-p under different photoexcitation and bias conditions. At zero bias ($V = 0$, first row, Figure 4e, h, i,

and j), the bands are flat everywhere in MoS₂, indicating that there are no electric fields; as a consequence, under excitation at 514 and 633 nm, photogenerated excitons in MoS₂ cannot be dissociated, and no photocurrent is produced. On the Si side, there is band bending (i.e., a built-in electric field) near the interface, which could potentially lead to charge separation and photocurrent if the carriers are photogenerated within the depletion layer. Thus, the absence of photoresponse under 785 nm excitation (Figure 4b) strongly suggests that there is an energy barrier that prevents the electrons from drifting into the MoS₂ layer, i.e., the CB edge of the MoS₂ layer is higher than that of Si. Furthermore, the fact that there is a finite photocurrent when excitons are resonantly created at 1.9 eV in MoS₂ suggests that the value of the CB offset is at least larger than the exciton binding energy (which is 0.2–0.4 eV³⁶).

Under forward bias ($V > 0$) and 514 and 633 nm excitation (second row, Figure 4f, k, and l), there is now an in-plane electric field, which separates electrons and holes, driving electrons (holes) in the positive z (x) direction. Note, however, that the electric field created by the external bias is not large enough to directly ionize the excitons in MoS₂, and the actual ionization mechanism (which may involve some pre-existing local electric fields) is not understood at this point. No matter what the microscopic exciton ionization mechanism is, the application of a finite external bias voltage leads to charge collection and finite photocurrent signal, as seen in Figure 4b. More specifically, the photoelectrons generated in the MoS₂ monolayer cross the MoS₂–Si interface and reach the bottom electrode, while the photoholes move in the lateral direction within the MoS₂ monolayer and finally reach the top electrode. Under reversed bias, the directions of the movement of the photoelectrons and photoholes are reversed compared to the forward bias case (third row, Figure 4g, n, and o). For 785 nm excitation under bias, however, there is still no photoresponse (Figure 4b). This indicates (see the third column, Figure 4m and p) that the conduction band barrier always exists irrespective of the sign and amplitude of the applied bias, again consistent with the notion that the band alignment between MoS₂ and Si is type I; i.e., the CB bottom of MoS₂ is higher than that of Si. Overall, these band diagrams provide qualitative accounts for the observed wavelength and bias dependence of the photocurrent.

Finally, we performed time-resolved photocurrent measurements with a 543 nm CW laser whose amplitude was modulated. The falling edge of the photocurrent, recorded by an oscilloscope, is shown in Figure 5a at a reversed bias (–2 V). We observe an immediate decrease of photocurrent after blocking the laser (“off” status in Figure 5a), followed by a slow decay. Curve fitting of the slow decay signal to an exponential function suggests a time constant (τ) of 159.2 s (Figure 5b). The rapid decrease with the reversed bias can be attributed to relaxation of charge carriers via recombination, while the slow decay might be attributed to the existence of trap sites at the heterojunction that could contribute to ultrahigh external quantum efficiencies in 2D material heterojunctions.³⁷ To acquire further information on the fast decay, we used a mechanical chopper to modulate the laser amplitude at a frequency of 600 Hz; as shown in Figure 5c, the square shape can be well-maintained (Figure 5c). The time constant (τ) is 12.3 μ s (8.06×10^4 Hz) calculated by exponential curve fitting of the first falling edge (Figure 5d). The speed of MoS₂–Si photodetector is comparable to or better than some of the

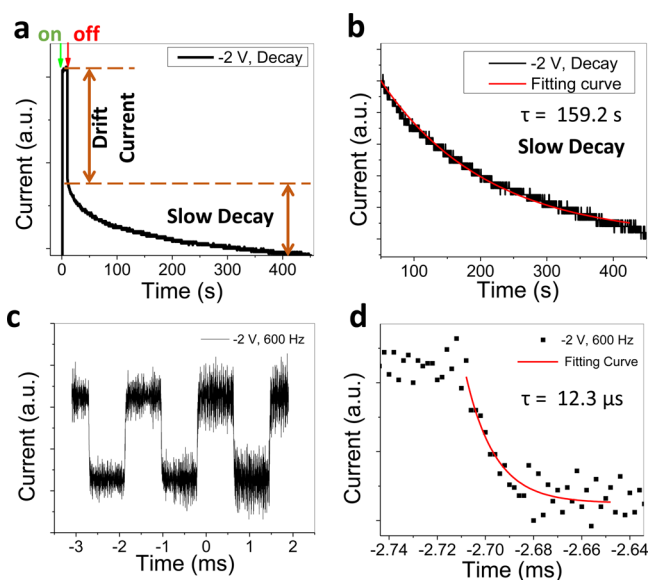


Figure 5. Time-resolved photoresponse of MoS₂–Si heterojunction. (a) Time-resolved photoresponse with reverse bias, –2 V, and (b) curve fitting of the slow decay. The time constant, τ , is calculated to be 159.2 s. “On” and “off” suggest the exposure status of the 543 nm CW laser beam on the heterojunction. (c) Time-resolved photoresponse measurements with an amplitude-modulated laser with reverse bias (–2 V) and 600 Hz chopping frequency and (d) exponential curve fitting of the first falling edge in c. The time constant, τ , is calculated to be 12.3 μ s.

fastest photodetectors based on 2D semiconductors reported so far^{26,38,39} (Supporting Information, Figure S3).

It is important to note that, with the progress of large-scale CVD-grown layered semiconductors, these heterodevices are fully scalable and tunable. As can be seen in Figure 3, the whole junction area is photosensitive, suggesting the performance of the device is scalable with the area of the junction. We have also shown that the photoresponse of the junction such as the photocurrent, photoconductivity, and the external quantum efficiency can be controlled by excitation intensity and external bias (Supporting Information, Figure S4).

In summary, our experiments increase the understanding of a novel heterojunction between an n-type 2D material, monolayer MoS₂, and p-type bulk Si. There are several key findings that can guide the future design of this type of photodetectors. For the first time, a band diagram that takes into consideration all three spatial dimensions of the device was constructed. We believe that this scheme provides a new angle from which to understand the optoelectronic properties of junctions containing 2D materials, including not only 2D–3D heterojunctions with different combinations of semiconductors, but also heterojunctions between different 2D materials. It was seen that the performance of the heterojunction was mainly dependent on the electron–hole pair excitation and collection in the monolayer part of the junction. Wavelength-dependent measurements strongly suggest type I band alignment for this heterojunction. We also revealed high-speed and low-speed components in the photoresponse of the MoS₂–Si junction, suggesting that high-speed photodetectors or low-speed devices can be constructed based on the same junction, but utilizing distinct response frequency regimes. Our understanding of the 2D–3D semiconductor heterojunctions will pave the way for the design of new low-dimensional optoelectronic devices.

Methods. The instruments used for material characterization include: an atomic force microscopy system (Bruker multimode 8) for thin-film thickness measurements; an aberration-corrected Nion UltraSTEM-100 operating at 60 kV for high-resolution scanning transmission electron microscopy; and a Renishaw inVia Raman spectroscopy system for Raman spectroscopy and photoluminescence spectroscopy analysis. Time-resolved photocurrent mapping was performed in a custom data collecting system with a 543 nm laser generator, a mechanical chopper, a source meter (Keithley 2643), and an oscilloscope (Tektronix TDS 2024C). The photocurrent mapping setup was composed with a CW lasers (514 nm) focused to $\sim 2 \mu\text{m}$, a stepper motor, and a source meter (Keithley 2400).

■ ASSOCIATED CONTENT

Supporting Information

The Supporting Information is available free of charge on the ACS Publications website at DOI: 10.1021/acs.nanolett.5b02012.

An optical image of MoS₂-Si junction; Raman spectrum of MoS₂-Si; the falling and rising time of photoresponse with laser modulated at the frequency of 600 Hz; the photoresponse of MoS₂-Si heterojunction under the exposure of a 514 nm laser with different light exposure intensities (PDF)

■ AUTHOR INFORMATION

Corresponding Authors

*E-mail: kono@rice.edu.

*E-mail: robert.vajtai@rice.edu.

*E-mail: ajayan@rice.edu.

Author Contributions

B.L., G.S., and S.L. contributed equally to this work. B.L., R.V., and P.M.A. conceived the concept and designed the experiment. G.S. and W.G. performed wavelength-dependent photocurrent measurements, and G.S. generated photocurrent maps. S.L. carried out the time-resolved and wavelength-dependent photocurrent measurements. Y.H. prepared samples and performed photoluminescence mapping and Raman spectroscopy measurements. Y.G. and G.Y. synthesized the MoS₂ flakes and prepared the MoS₂-Si heterostructures devices. W.Z. performed STEM imaging. K.K., J.H., P.D., L.G., and J.L. helped to analyze the experimental results. B.L., S.L., R.V., and J.K. developed the band diagrams. The manuscript was written by B.L., G.S., S.L., W.G., J.K., R.V., and P.M.A., with comments and input from all authors.

Funding

This work was funded by FAME, one of six centers of STARnet, a Semiconductor Research Corporation program sponsored by MARCO and DARPA, MURI ARO program, grant number W911NF-11-1-036, and by the Air Force Office of Scientific Research under Award Number FA9550-14-1-0268.

Notes

The authors declare no competing financial interest.

■ ACKNOWLEDGMENTS

We thank Ali Sobhani, Naomi Halas, Gary Woods, and Alexey Belyanin for helpful discussions. W.Z. acknowledges support from the U.S. Department of Energy, Office of Science, Basic

Energy Sciences, Materials Sciences and Engineering Division, and a user project at ORNL's Center for Nanophase Materials Sciences (CNMS), which is a DOE Office of Science User Facility.

■ REFERENCES

- (1) Geim, A.; Grigorieva, I. *Nature* **2013**, *499* (7459), 419–425.
- (2) Lee, C.-H.; Lee, G.-H.; van der Zande, A. M.; Chen, W.; Li, Y.; Han, M.; Cui, X.; Arefe, G.; Nuckolls, C.; Heinz, T. F.; Guo, J.; Hone, J.; Kim, P. *Nat. Nanotechnol.* **2014**, *9*, 676–681.
- (3) Koppens, F.; Mueller, T.; Avouris, P.; Ferrari, A.; Vitiello, M.; Polini, M. *Nat. Nanotechnol.* **2014**, *9* (10), 780–793.
- (4) Wang, Q. H.; Kalantar-Zadeh, K.; Kis, A.; Coleman, J. N.; Strano, M. S. *Nat. Nanotechnol.* **2012**, *7* (11), 699–712.
- (5) Coleman, J. N.; Lotya, M.; O'Neill, A.; Bergin, S. D.; King, P. J.; Khan, U.; Young, K.; Gaucher, A.; De, S.; Smith, R. J. *Science* **2011**, *331* (6017), 568–571.
- (6) Mak, K. F.; Lee, C.; Hone, J.; Shan, J.; Heinz, T. F. *Phys. Rev. Lett.* **2010**, *105* (13), 136805.
- (7) Radisavljevic, B.; Radenovic, A.; Brivio, J.; Giacometti, V.; Kis, A. *Nat. Nanotechnol.* **2011**, *6* (3), 147–150.
- (8) Najmaei, S.; Liu, Z.; Zhou, W.; Zou, X. L.; Shi, G.; Lei, S. D.; Yakobson, B. I.; Idrobo, J. C.; Ajayan, P. M.; Lou, J. *Nat. Mater.* **2013**, *12* (8), 754–759.
- (9) Britnell, L.; Ribeiro, R.; Eckmann, A.; Jalil, R.; Belle, B.; Mishchenko, A.; Kim, Y.-J.; Gorbachev, R.; Georgiou, T.; Morozov, S. *Science* **2013**, *340* (6138), 1311–1314.
- (10) Williams, J.; DiCarlo, L.; Marcus, C. *Science* **2007**, *317* (5838), 638–641.
- (11) Gong, Y.; Lin, J.; Wang, X.; Shi, G.; Lei, S.; Lin, Z.; Zou, X.; Ye, G.; Vajtai, R.; Yakobson, B. I. *Nat. Mater.* **2014**, *13*, 1135–1142.
- (12) Huang, C.; Wu, S.; Sanchez, A. M.; Peters, J. J.; Beanland, R.; Ross, J. S.; Rivera, P.; Yao, W.; Cobden, D. H.; Xu, X. *Nat. Mater.* **2014**, *13* (12), 1096–1101.
- (13) Duan, X.; Wang, C.; Shaw, J. C.; Cheng, R.; Chen, Y.; Li, H.; Wu, X.; Tang, Y.; Zhang, Q.; Pan, A. *Nat. Nanotechnol.* **2014**, *9*, 1024–1030.
- (14) Ross, J. S.; Klement, P.; Jones, A. M.; Ghimire, N. J.; Yan, J.; Mandrus, D.; Taniguchi, T.; Watanabe, K.; Kitamura, K.; Yao, W. *Nat. Nanotechnol.* **2014**, *9* (4), 268–272.
- (15) Pospischil, A.; Furchi, M. M.; Mueller, T. *Nat. Nanotechnol.* **2014**, *9*, 257–261.
- (16) Lei, S.; Sobhani, A.; Wen, F.; George, A.; Wang, Q.; Huang, Y.; Dong, P.; Li, B.; Najmaei, S.; Bellah, J.; Ajayan, P. M. *Adv. Mater.* **2014**, *26*, 7666–7672.
- (17) Lei, S.; Ge, L.; Liu, Z.; Najmaei, S.; Shi, G.; You, G.; Lou, J.; Vajtai, R.; Ajayan, P. M. *Nano Lett.* **2013**, *13* (6), 2777–2781.
- (18) Li, L.; Yu, Y.; Ye, G. J.; Ge, Q.; Ou, X.; Wu, H.; Feng, D.; Chen, X. H.; Zhang, Y. *Nat. Nanotechnol.* **2014**, *9*, 372–377.
- (19) Lei, S.; Wen, F.; Li, B.; Wang, Q.; Huang, Y.; Gong, Y.; He, Y.; Dong, P.; Bellah, J.; George, A.; Ge, L.; Lou, J.; Halas, N. J.; Vajtai, R.; Ajayan, P. M. *Nano Lett.* **2015**, *15*, 259–265.
- (20) Fontana, M.; Deppe, T.; Boyd, A. K.; Rinzan, M.; Liu, A. Y.; Paranjape, M.; Barbara, P. *Sci. Rep.* **2013**, *3*, 1634.
- (21) An, Y.; Behnam, A.; Pop, E.; Ural, A. *Appl. Phys. Lett.* **2013**, *102* (1), 013110.
- (22) Bonaccorso, F.; Colombo, L.; Yu, G.; Sotiller, M.; Tozzini, V.; Ferrari, A. C.; Ruoff, R. S.; Pellegrini, V. *Science* **2015**, *347* (6217), 1246501.
- (23) Li, X.; Zhu, H.; Wang, K.; Cao, A.; Wei, J.; Li, C.; Jia, Y.; Li, Z.; Li, X.; Wu, D. *Adv. Mater.* **2010**, *22* (25), 2743–2748.
- (24) An, X.; Liu, F.; Jung, Y. J.; Kar, S. *Nano Lett.* **2013**, *13* (3), 909–916.
- (25) Lopez-Sanchez, O.; Alarcon Llado, E.; Koman, V.; Fontcuberta i Morral, A.; Radenovic, A.; Kis, A. *ACS Nano* **2014**, *8*, 3042–3048.
- (26) Esmaili-Rad, M. R.; Salahuddin, S. *Sci. Rep.* **2013**, *3*, 2345.

- (27) Tsai, M.-L.; Su, S.-H.; Chang, J.-K.; Tsai, D.-S.; Chen, C.-H.; Wu, C.-L.; Li, L.-J.; Chen, L.-J.; He, J.-H. *ACS Nano* **2014**, *8*, 8317–8322.
- (28) Yim, C.; O'Brien, M.; McEvoy, N.; Riazimehr, S.; Schäfer-Eberwein, H.; Bablich, A.; Pawar, R.; Iannaccone, G.; Downing, C.; Fiori, G. *Sci. Rep.* **2014**, *4*, 5458.
- (29) Hao, L.; Liu, Y.; Gao, W.; Han, Z.; Xue, Q.; Zeng, H.; Wu, Z.; Zhu, J.; Zhang, W. *J. Appl. Phys.* **2015**, *117* (11), 114502.
- (30) Ye, Y.; Ye, Z.; Gharghi, M.; Zhu, H.; Zhao, M.; Wang, Y.; Yin, X.; Zhang, X. *Appl. Phys. Lett.* **2014**, *104* (19), 193508.
- (31) Li, Y.; Xu, C.-Y.; Wang, J.-Y.; Zhen, L. *Sci. Rep.* **2014**, *4*, 7186.
- (32) Chiu, M.-H.; Zhang, C.; Shiu, H. W.; Chuu, C.-P.; Chen, C.-H.; Chang, C.-Y. S.; Chen, C.-H.; Chou, M.-Y.; Shih, C.-K.; Li, L.-J. *arXiv* **2014**, 1406.5137.
- (33) Kang, J.; Tongay, S.; Zhou, J.; Li, J.; Wu, J. *Appl. Phys. Lett.* **2013**, *102* (1), 012111.
- (34) Sze, S. M. *Semiconductor devices: physics and technology*; John Wiley & Sons: Wiley, 2008.
- (35) Furchi, M. M.; Pospischil, A.; Libisch, F.; Burgdörfer, J.; Mueller, T. *Nano Lett.* **2014**, *14* (8), 4785–4791.
- (36) Zhang, C.; Johnson, A.; Hsu, C.-L.; Li, L.-J.; Shih, C.-K. *Nano Lett.* **2014**, *14* (5), 2443–2447.
- (37) Lopez-Sanchez, O.; Lembke, D.; Kayci, M.; Radenovic, A.; Kis, A. *Nat. Nanotechnol.* **2013**, *8*, 497–501.
- (38) Buscema, M.; Groenendijk, D. J.; Blanter, S. I.; Steele, G. A.; van der Zant, H. S.; Castellanos-Gomez, A. *Nano Lett.* **2014**, *14* (6), 3347–3352.
- (39) Tsai, D.-S.; Liu, K.-K.; Lien, D.-H.; Tsai, M.-L.; Kang, C.-F.; Lin, C.-A.; Li, L.-J.; He, J.-H. *ACS Nano* **2013**, *7* (5), 3905–3911.